A MEMS Singlet Oxygen Generator—Part I: Device Fabrication and Proof of Concept Demonstration

Luis Fernando Velásquez-García, Tyrone F. Hill, Benjamin A. Wilhite, Klavs F. Jensen, Alan H. Epstein, *Member, ASME*, and Carol Livermore, *Member, IEEE*, *Member, ASME*

***Abstract*—This paper reports the design, fabrication, and proof of concept demonstration of a singlet oxygen generator (SOG) that operates on the microscale. The micro-SOG (μSOG) chip is implemented in a three-wafer stack using deep reactive ion etching (DRIE) and wafer bonding as key technologies. The device creates singlet delta oxygen ($O_2(a)$) in an array of packed-bed reaction channels fed by inlet manifolds with pressure drop channels that ballast the flow. An integrated capillary array separates the liquid and gas by-products, and a microscale heat exchanger removes excess heat of reaction. The fabrication process and package are designed to minimize collisional losses and wall deactivation of $O_2(a)$. The design, fabrication, and package of the device are documented. Proof of concept demonstration of the device is given by optical emission measurements of the spontaneous decay of the $O_2(a)$ molecule into its triplet state and by the observation of the emission from dimol pairs of $O_2(a)$ molecules. [2007-0034]**

***Index Terms*—Chemical oxygen–iodine laser (COIL), deep reactive ion etching (DRIE), microfluidics, singlet oxygen.**

I. Introduction

An OXYGEN molecule has four electrons in its outer p-subshell. The $O_2(X^3\Sigma^-)$ state (also known as triplet oxygen, ground-state oxygen, or $O_2(X)$) has three electrons in one spin state and the fourth in the other, whereas the $O_2(a^1\Delta_g)$ state (also known as singlet delta oxygen, spin-excited molecular oxygen, or $O_2(a)$) has two electrons in each of the "spin up" and "spin down" configurations [1]. Singlet delta oxygen is valuable as a reactant for organic synthesis and as an energy carrier for the chemical oxygen–iodine laser (COIL). COIL is attractive for applications that require very high average power, light weight, and overall system compactness, and it provides a promising alternative to CO_2 lasers for industrial machining. A lower emission wavelength (1.315 versus 10.6 μm for CO_2) results in more efficient coupling to metals, reducing the power needed for welding and cutting. The lower wavelength also results in a smaller spot size, so COIL systems offer higher machining resolution and enable fiber-optic beam delivery for greater flexibility. In a flowing gas laser such as COIL, the waste heat flows out with the exhaust gas stream; therefore, the laser's average power is not limited by cooling, as are most high-energy solid-state lasers.

COIL systems are chemical lasers in which iodine acts as the lasing species [2]. Population inversion of the gain medium is sustained by collisions between ground-state iodine atoms ($I(^2P_{3/2})$) and $O_2(a)$, i.e., COIL is a two-species two-level laser, where the near resonance between the $O_2(a)$ state and the $I(^2P_{1/2})$ state of atomic iodine makes $O_2(a)$ an ideal pumping source for laser emission. $O_2(a)$ is metastable and may be synthesized through the highly exothermic multiphase reaction of gaseous Cl_2 with an aqueous mixture of concentrated H_2O_2 and KOH, which is commonly referred to as basic hydrogen peroxide (BHP). Usually, the reactant Cl_2 is buffered with a nonreacting gas such as helium. The laser application of $O_2(a)$ generation requires a high yield to sustain laser emission, where yield is defined as the fraction of product oxygen in the $O_2(a)$ state. The laser application also requires high conversion of Cl_2 to $O_2(a)$, which is achieved by effective mixing of the gas and liquid reagents.

Once produced, $O_2(a)$ may deactivate into ground-state oxygen by gas-phase collisions with water vapor or with other oxygen or helium molecules, or by heterogeneous collisions with solid surfaces. Thus, the reactor design must provide large surface areas for initial $O_2(a)$ generation, followed by rapid separation of gas and liquid phases. The output gas must be maintained at low pressures ($\sim$50–250 torr) to minimize homogeneous deactivation, and the reactor must be maintained at low temperatures ($< 0\,^\circ$C) to minimize water vaporization and the resulting iodine deactivation that water vapor would cause in a complete COIL system. This paper shows that the challenges of high yield, thermal management, and product separation can be successfully addressed by a MEMS-based approach to $O_2(a)$ generation.

Generation of $O_2(a)$ for COIL was first demonstrated by McDermott *et al.* in 1978 [2]. A 6000-sccm flow of Cl_2 gas was bubbled through an aqueous solution of 90 wt% H_2O_2 and 6 M NaOH in a dry ice and ethanol-cooled sparger, producing $O_2(a)$. A cold trap removed moisture and unreacted chlorine

Manuscript received February 7, 2007; revised May 21, 2007. This work was supported in part by the Tactical Technology Office at the Defense Advanced Research Projects Agency (DARPA), in part by the Missile Defense Agency (MDA), and in part by the Air Force Research Laboratory through DARPA Order T171/00, Program Code: 4G10, issued by the DARPA Contracts Management Office under Contract MDA972-04-C-0140. Subject Editor A. Ricco.

L. F. Velásquez-García is with the Microsystems Technology Laboratories and the Gas Turbine Laboratory, Massachusetts Institute of Technology, Cambridge, MA 02139 USA (e-mail: lfvelasq@mit.edu).

T. F. Hill is with the Department of Electrical Engineering and Computer Science, Massachusetts Institute of Technology, Cambridge, MA 02139 USA.

K. F. Jensen and A. H. Epstein are with the Massachusetts Institute of Technology, Cambridge, MA 02139 USA.

C. Livermore is with the Department of Mechanical Engineering, Massachusetts Institute of Technology, Cambridge, MA 02139 USA (e-mail: livermor@mit.edu).

B. A. Wilhite is with the Department of Chemical Engineering, University of Connecticut, Storrs, CT 06269 USA.

Digital Object Identifier 10.1109/JMEMS.2007.902446

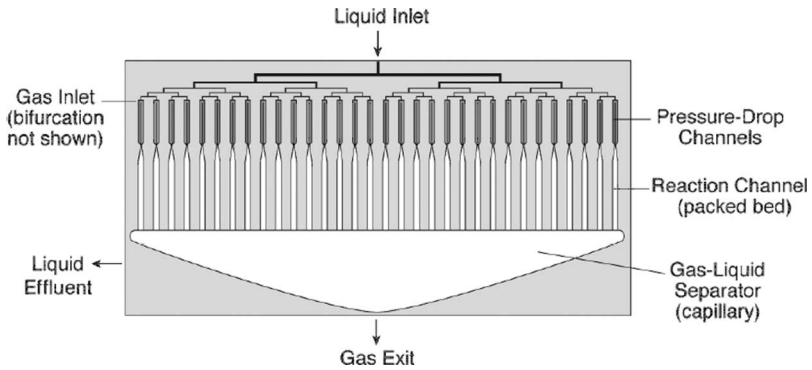

Fig. 1. Schematic of the μSOG. The system also has a microfabricated heat exchanger (not shown) directly below the reaction channels to control the chip temperature.

from the product gas before mixing it with I_2 and Ar. The $O_2(a)$ yield was approximately 40%. McDermott *et al.*'s method was successful, but it is limited by significant deactivation of the $O_2(a)$ gas before its separation from the liquid phase. Subsequent singlet oxygen generator (SOG) configurations have employed either jets of BHP droplets mixed with Cl_2 [3] or rotating-disk configurations [4]. In rotating-disk SOGs, a film of BHP on the surface of a rotating wheel is exposed to a Cl_2 stream, resulting in $O_2(a)$ production at the interface. However, these configurations also have limitations: a small gas–liquid contact area for rotary SOGs and a large volume for the jet configuration.

Modeling suggests that a COIL that utilizes MEMS components has key advantages as compared with fully macroscale implementations. These advantages include smaller hardware size for the same power level, more efficient reactant utilization, gravity independence, and feasible batch manufacturing [5]. This paper demonstrates successful generation of $O_2(a)$ in a MEMS-based SOG chip, and it suggests that arrays of MEMS-based SOGs can address the shortcomings of macroscale SOG designs, thus providing higher yields and a greater $O_2(a)$ flow per unit reactor volume. The advantages of the MEMS-based SOG reported here are enabled by a set of key device characteristics, which may be summarized as follows. First, the MEMS-based SOG has a large surface-to-volume ratio, which enhances reactant mixing and facilitates excess heat removal, as demonstrated in previous gas–liquid reactions in microreactors [6]. Second, the device has no moving parts, which increases the robustness and reliability of the system. Third, $O_2(a)$ travels a shorter distance from the point of formation to the point of utilization in the microdevice, thus reducing $O_2(a)$ losses. Fourth, the integration of a microfabricated heat exchanger in the micro-SOG (μSOG) chip simplifies the overall COIL system. Fifth, a capillary gas–liquid separator permits orientation-independent operation or even operation in zero gravity. The final enabling characteristic is the ability to efficiently and scalably manufacture COIL components through batch fabrication.

Section II presents a conceptual discussion of SOG operation and details of the device structure. In Section III, the process flow and fabrication characterization of the device are documented. In Section IV, the package is described. In Section V, experimental results that confirm the production of singlet delta oxygen are presented as a proof of concept demonstration.

II. SOG Concept and Structure

SOGs typically produce $O_2(a)$ by mixing gaseous chlorine and BHP, according to the overall chemical reaction

$$H_2O_2 + 2KOH + Cl_2 \rightarrow 2H_2O + 2KCl + O_2(a). \quad (1)$$

Often, the Cl_2 is mixed with a buffer gas (He or N_2) in order to raise the total pressure of the stream. After generation, $O_2(a)$ may be deactivated by several mechanisms, with the most prominent being collisions between $O_2(a)$ molecules, i.e.,

$$O_2(a) + O_2(a) \rightarrow O_2(b) + O_2(X) \quad (2)$$

$$O_2(a) + O_2(a) \rightarrow O_2(X) + O_2(X) \quad (3)$$

where $O_2(b)$ refers to the excited $O_2(b^1\Sigma_g^+)$ state of oxygen, and wall interactions, i.e.,

$$O_2(a) + \text{wall} \rightarrow O_2(X). \quad (4)$$

The reaction rate is limited by [and the subsequent $O_2(a)$ deactivation depends on] the transport of gaseous chlorine into and gaseous $O_2(a)$ out of the liquid phase. Therefore, maximizing the gas–liquid contact area is critical both to promote the reaction and to obtain a high $O_2(a)$ yield.

Fig. 1 shows a schematic of the μSOG chip. The system is composed of 32 packed-bed reaction channels that are fed in parallel with the gas and liquid reactants using bifurcating manifolds. The reactants mix inside the reactor beds. Chlorine diffuses into the BHP, where it reacts to produce $O_2(a)$. The $O_2(a)$ then diffuses back out into the flow of gas. The packed bed has a staggered configuration that increases mixing of the laminar reactant flows by increasing the vorticity without moving parts. Pressure-drop channels that are located upstream of each packed bed equalize flows among the reaction channels of the microdevice, thus acting as hydraulic impedances that ballast the reactor array. The reactor design builds upon and extends previous gas–liquid microreactors for oxidizing organic liquids with the highly reactive ozone gas [7]. The reaction channels flow into a gas–liquid separator in which an array of capillaries removes the liquid by-products from the gaseous output stream. The $O_2(a)$ is then collected and routed to the chip's gas outlet port. A previous analytical study evaluated the feasibility of microscale $O_2(a)$ generation [5].

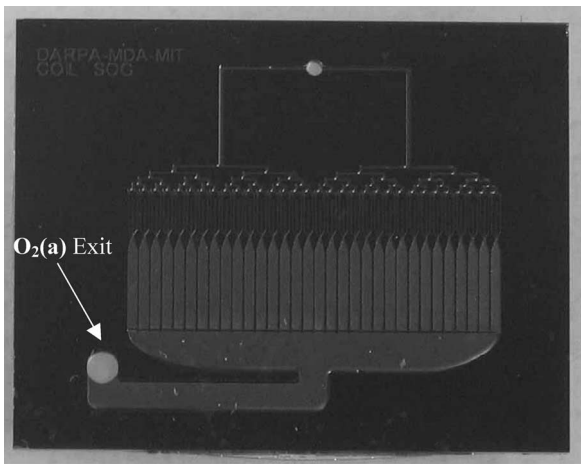

Fig. 2. Photograph of a completed μSOG chip, showing features that are similar to those that are represented in the schematic of Fig. 1. The singlet delta oxygen exit port is at the lower left-hand side of the chip.

Using standard MATLAB numerical simulation techniques and estimates of physical parameters, key SOG dimensions and operating points were optimized. The dimensions employed in the present μSOG mask design were largely based on the results and conclusions of this study. The optimum device dimensions from the study (given the estimated parameters) included 0.516-cm-long reaction channels, 0.25-cm-long pressure drop channels, a 1-cm section for gas and liquid flow distribution, and an optimal total gas (helium plus chlorine) flow rate of 175 sccm at a $3:1$ He:Cl_2 ratio.

Fig. 2 is a photograph of a completed μSOG chip made as a three-wafer stack. Fig. 3(a) shows a simplified 3D model of the μSOG. The top wafer is Pyrex and seals the flow channels while providing optical access to the reaction channels and separator. The middle wafer is silicon and contains the distribution manifold for the liquid reactants, the pressure drop channels, the capillary separator, and the packed-bed reaction channels. The pressure drop channels have a width of 25 μm and a depth of 20 ± 1 μm. The BHP pressure drop channels are 2750 ± 50 μm long, and the gas pressure drop channels are 2428 ± 35 μm long. In both cases, the aspect ratio is larger than 100, and the pressure drop channels' hydraulic diameter is about 22 μm. The reaction channels are each 6.1 mm long, 630 μm wide, and 360 μm high; the length was increased above the optimized length given above to ensure adequate residence time for complete reaction of the chlorine. Each reactor packed bed contains a hexagonal array of columns with 340 μm height, 70 μm diameter, and 90 μm pitch. This post bed configuration is a 2-D approximation of a conventional packed bed, providing reduced pressure drops while eliminating the need for subsequent packing of reaction channels. The separator is composed of a hexagonal array of more than 7000 capillary holes with 265 μm length, 25 μm diameter, and 90 μm pitch that relies on surface tension effects to separate the two-phase exit stream [8]. There is a wide range of separator dimensions that is expected to be able to separate the exit stream; the set of dimensions used here ensures that the separator's flow capacity exceeds the anticipated flow rates. The hexagonal packing maximizes the feature density per unit area. Fig. 3(b) shows a cross section of

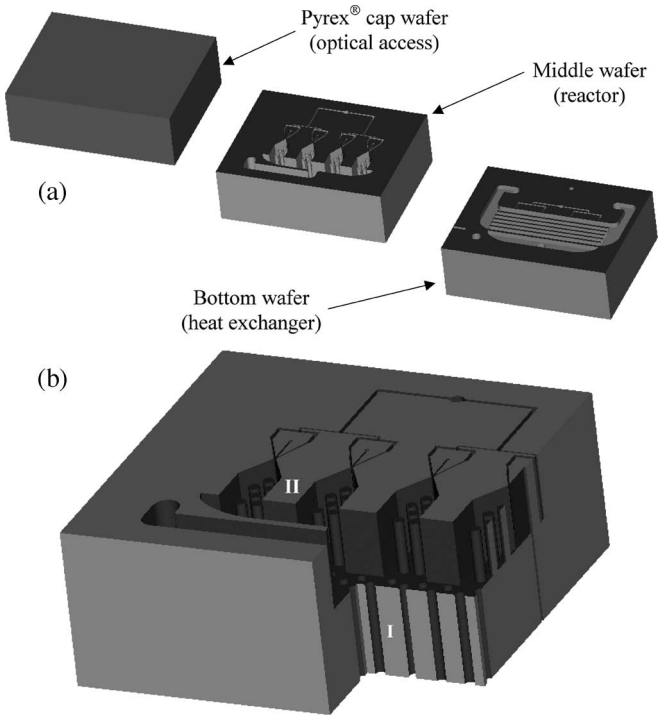

Fig. 3. Simplified 3-D model of the (a) μSOG chip with its constitutive layers and (b) cross section of the middle wafer. The middle wafer contains both (I) the capillary separator and (II) the packed-bed reaction channels.

the middle wafer. The bottom wafer is silicon and contains the distribution manifold for the gas reactants, the heat exchanger, and a port for an external thermocouple. The heat exchanger removes excess heat that is generated during the reaction, enabling low-temperature operation. The heat exchanger is made of 19 cooling channels, each of which is 23.9 mm long, 300 μm wide, and 300 μm deep. The BHP and Cl_2 inlets are 1 mm in diameter; all other inlet and outlet connections are 2 mm in diameter. The die size was set at 3.6×2.8 cm to accommodate packaging. Fig. 4(a) shows a photograph of a microfabricated middle wafer die, and Fig. 4(b) shows a photograph of a microfabricated bottom wafer die. All ports are on the back of the three-wafer stack to facilitate packaging and testing.

III. Fabrication

The fabrication process for the μSOG is intended to address the need for uniform flow rates across the chip (particularly reactor bed uniformity and capillary separator uniformity) and chemical inertness of the chip to BHP, chlorine, and singlet delta oxygen. Described broadly, the process flow heavily relies on deep reactive ion etching (DRIE), fusion bonding, and anodic bonding to build the device and uses a conformal layer of low-pressure chemical vapor deposition (LPCVD) silicon-rich nitride to protect the bulk silicon from the reactants and products. However, the successful creation of the μSOG chip critically depends on the details of the process flow, which ensure that three key requirements are met. First, different types of high-aspect-ratio features (posts and pores) must be created in the same process steps as features that have vastly different aspect ratios and in-plane dimensions. Second, the

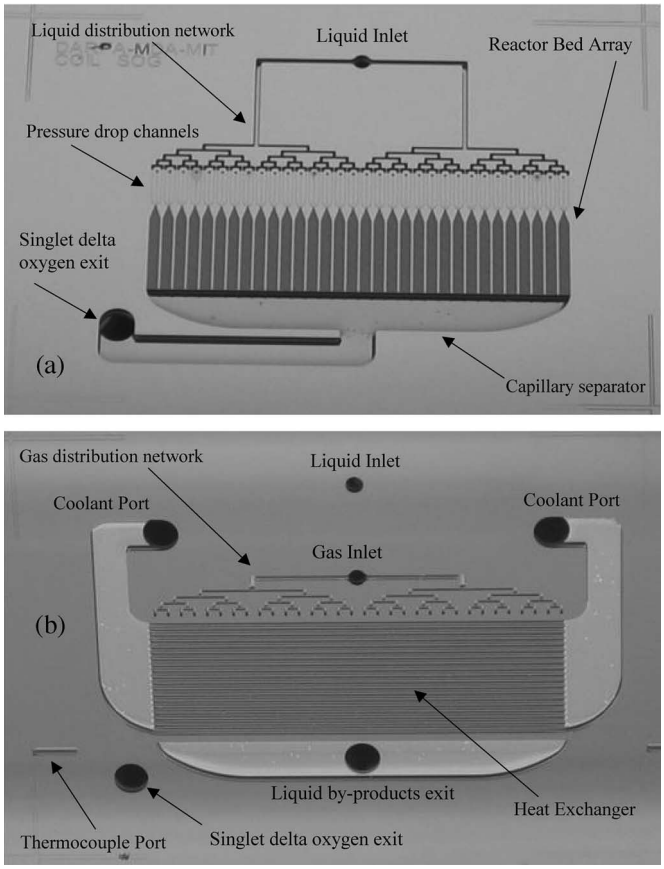

Fig. 4. Photographs of (a) the middle wafer and (b) the bottom wafer of a μSOG chip.

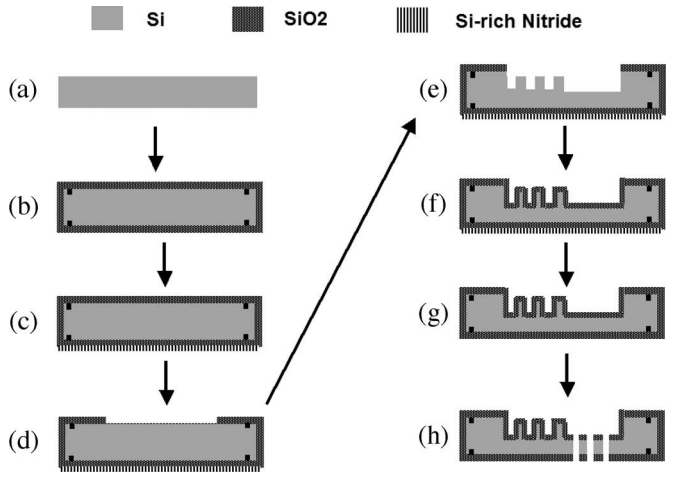

Fig. 5. Process flow by which the middle wafer of the μSOG is fabricated. The process flow starts with a DSP p-Si $\langle 100 \rangle$ wafer (a). The wafer is oxidized, and alignment marks are transferred to both sides of the wafer (b). The wafer is then coated with 0.5 μm of LPCVD silicon-rich silicon nitride, and the film on the top of the wafer is stripped using an RIE step (c). The silicon oxide film on the top surface of the wafer is patterned with the layouts of the pressure drop channels, the liquid inlet manifold, the reaction channels without the packed beds, and the region occupied by the separator (d). The reactor packed beds and an opening in the region that the separator will eventually occupy are then patterned in a resist and etched by DRIE (e). The photoresist film is stripped, and the features etched on the silicon oxide film on the top surface of the wafer are transferred to the silicon substrate using a DRIE step, while etching 20 μm. The wafer is then oxidized (f), and the silicon-rich silicon nitride on the backside of the wafer is stripped using hot phosphoric acid (g). Finally, the layouts of the chip ports and the capillary separator are patterned in a resist on the back side of the wafer, are transferred into the back-side silicon oxide layer with BOE, and are transferred to the silicon with DRIE. The photoresist film is stripped (h).

pattern definition and transfer techniques must permit wafer processing even after the removal of significant portions of the bulk silicon. Third, the assembly procedures must ensure that the silicon is entirely covered by a defect-free chemically inert coating of silicon nitride in order to prevent the dissolution of the μSOG chip upon exposure to BHP. The process flow for the μSOG, including the enabling details, is described in Section III-A; the fabrication characterization is described in Section III-B.

A. Process Flow

The device is made up of three 6-in wafers: one 2-mm-thick Pyrex wafer (Bullen Ultrasonics, Eaton, OH) and two 625 ± 20-μm-thick double-side-polished (DSP) p-Si $\langle 100 \rangle$ wafers (Silicon Quest, San Jose, CA). The Pyrex wafer is 2 mm thick for greater stiffness and higher pressure capability, but devices with Pyrex wafers that are 625 μm thick were also successfully fabricated and tested. The following is the process flow for the μSOG.

1) Middle Wafer: Fig. 5 shows a schematic of the process flow for the middle wafer. The middle wafer starts as a 625-μm-thick lightly doped DSP p-Si 6-in wafer (a). First, 0.5 μm of thermal silicon oxide is grown on the wafer, and alignment marks are transferred to front and back (b). The silicon oxide film protects the wafer surfaces for later fusion bonding. A 0.5-μm-thick silicon-rich LPCVD silicon nitride film is deposited to serve as a diffusion barrier for the future oxidation in step (f). If the nitride layer were omitted, any nonuniformities in the thickness of the oxide brought on by processing could be amplified by the subsequent oxidation, compromising the flatness of the bonding surface. The silicon-rich silicon nitride film is stripped from the wafer's top surface using an SF_6-based recipe on a LAM 490-B RIE plasma etcher (c). The wafer top then receives a nested mask to form the deep features (reaction channels, the liquid reactants manifold, and the capillary separator region) and the shallow features (pressure drop channels). The features to be patterned in the oxide mask layer (the liquid distribution network, pressure drop channels, reaction channels without the columns, and the region that will contain the capillary separator) are patterned in a 10-μm-thick AZ P4620 resist on the top of the wafer with contact photolithography. The back side of the wafer is protected with a photoresist, and the patterns are transferred to the oxide with a sonicated buffered oxide etch (BOE). The photoresist is stripped with piranha and oxygen plasma (d). The features to be patterned in the resist mask layer (reaction channels and capillary separator region) are transferred to a 10-μm-thick AZ P4620 photoresist layer. Using the patterned resist as a mask, an optimized DRIE step etches 340 μm of silicon anisotropically to form the packed-bed reaction channels and define the thickness of the remaining silicon where the capillary pores of the separator will ultimately be formed. The resist mask is stripped with oxygen plasma, and the silicon exposed by the oxide mask is etched with DRIE to pattern the pressure drop channels, pattern the liquid inlet manifold, and

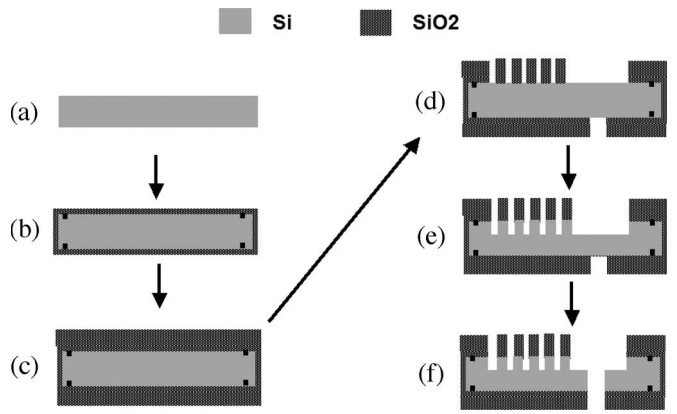

Fig. 6. Process flow that fabricates the bottom wafer of the μSOG. (a) The process flow starts with a DSP p-Si $\langle 100 \rangle$ wafer. (b) The wafer is oxidized, and alignment marks are transferred to both sides of the wafer. The wafer is then coated with 4 μm of PECVD silicon oxide on both sides of the wafer and annealed at 950 °C in a nitrogen atmosphere (c). The resist is applied to both sides of the wafer. The resist film on the top of the wafer is patterned photolithographically with the layouts of the heat exchanger and the gas inlet manifold, whereas the bottom film is patterned with the layouts of the chip ports. The layouts of both resist films are transferred to the silicon oxide films using a cycled RIE plasma recipe (d). The top of the wafer is then etched with DRIE to a depth of 325 μm (e). Finally, the wafer is flipped over and mounted on top of a quartz wafer, and the chip ports are etched with DRIE (f).

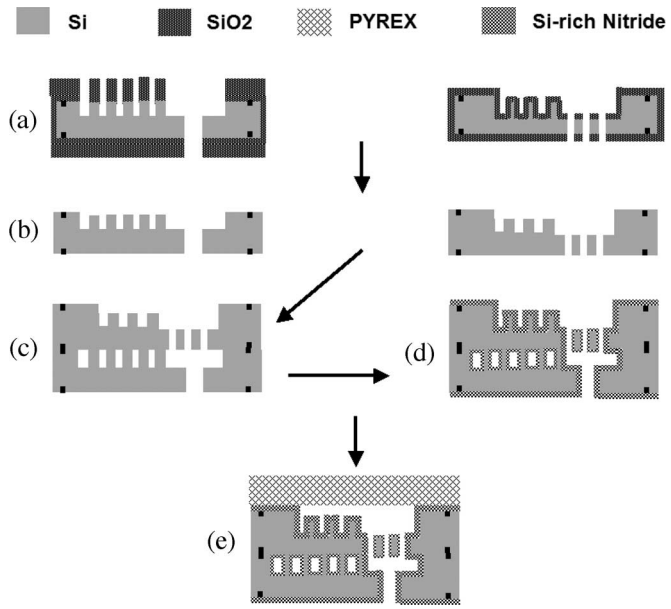

Fig. 7. Process flow to finalize the fabrication of the μSOG. The microfabricated middle and bottom wafers (a) are immersed in a 49% HF bath to strip the silicon oxide films (b). The two silicon wafers are fusion bonded (c). Then, a 0.4-μm-thick LPCVD silicon-rich nitride is conformally deposited on the silicon wafer stack (d). Next, the silicon wafer stack is anodically bonded to an unpatterned Pyrex wafer (e). The wafer stack is then die sawed to extract the SOG chips.

finish etching the packed-bed reaction channels to a total depth of 360 μm (e). The wafer is RCA cleaned and oxidized to grow 0.5 μm of silicon oxide on all exposed silicon surfaces. The silicon oxide protects the posts from any collateral damage during future DRIE processing (f). The silicon nitride is stripped using a hot phosphoric acid mixture at 165 °C (g). The wafer is then flipped over and attached to die saw tape to provide a removable sealable surface to the spin coater's vacuum chuck. The bottom of the wafer receives a 10-μm-thick AZ P4620 photoresist film with the layout of the chip ports and the capillary separator pores. The exposed oxide is removed in BOE, and the wafer is etched with DRIE to form the capillary separator (h). The wafer is dismounted, and the photoresist is stripped using piranha and oxygen plasma.

2) Bottom Wafer: Fig. 6 shows a schematic of the process flow for the bottom wafer. The bottom wafer starts as a 625-μm-thick lightly doped DSP p-Si 6-in wafer (a). First, 0.5 μm of thermal silicon oxide is grown on the wafer, and alignment marks are transferred to front and back (b). The silicon oxide film protects the wafer surfaces for later fusion bonding. Next, a 4-μm-thick plasma-enhanced chemical vapor deposition (PECVD) silicon oxide is deposited on both sides of the wafer, and the films are annealed for 1 h at 950 °C in nitrogen (c). After annealing, both sides of the wafer are coated with a 10-μm-thick AZ P4620 photoresist. The heat exchanger and gas inlet manifold are patterned in the front-side resist, and the chip ports (liquid and gas inlets and exits, including the coolant ports) are patterned in the back-side resist. The exposed oxide on both sides is anisotropically etched with a cycled $CHF_3C_2F_4$-based RIE plasma etch to form DRIE etch masks (d). The photoresist is stripped with piranha followed by oxygen plasma. The heat exchanger and gas inlet network are etched to a total depth of 315 μm with DRIE (e). The wafer is flipped over, mounted on a quartz handle wafer, and etched with DRIE to pattern the chip ports (f). The wafer is then dismounted from the quartz handle wafer.

3) Final Processing: Fig. 7 shows a schematic of the process flow that completes the device. The completed middle and bottom wafers are immersed in 49% hydrofluoric acid (HF) to strip the silicon oxide films and are then RCA cleaned, contacted, pressed with 2500 N of force for 12 h, and fusion bonded at 1050 °C for 1 h in nitrogen (a). The silicon wafer stack then goes directly to the LPCVD reactor to be coated with a 0.4-μm-thick conformal silicon-rich silicon nitride film (b). The silicon-rich silicon nitride film acts like a glove that protects the silicon substrate from the reactants and products, in particular, from the BHP. The stack is anodically bonded to an unpatterned Pyrex wafer for 10 min, using 1000 V_{DC}, a compressive force of 1000 N, and a bonding temperature of 350 °C (c). The wafer stack is then die sawed using a 250-μm-thick glass blade. Eight μSOG chips are obtained from each wafer stack, and a near 100% yield was achieved in all batches.

B. Fabrication Characterization

Fig. 8 is a set of SEM pictures that show cross sections of one of the μSOG chips. Key features such as the reactor packed beds, the cooling channels, the liquid by-products collector tray, and the capillary separator can be identified. Fig. 9(a) and (b) depicts SEM micrographs that show the structure of a reactor packed-bed channel. The as-fabricated columns have a diameter of 70 μm, an aspect ratio of 5, and a pitch of 90 μm. The roots of the columns have large radii to avoid fracture. Fig. 9(c) and (d) shows SEM micrographs that illustrate the capillary separator structure. The separator consists of 25-μm-diameter capillary holes on a 90-μm pitch.

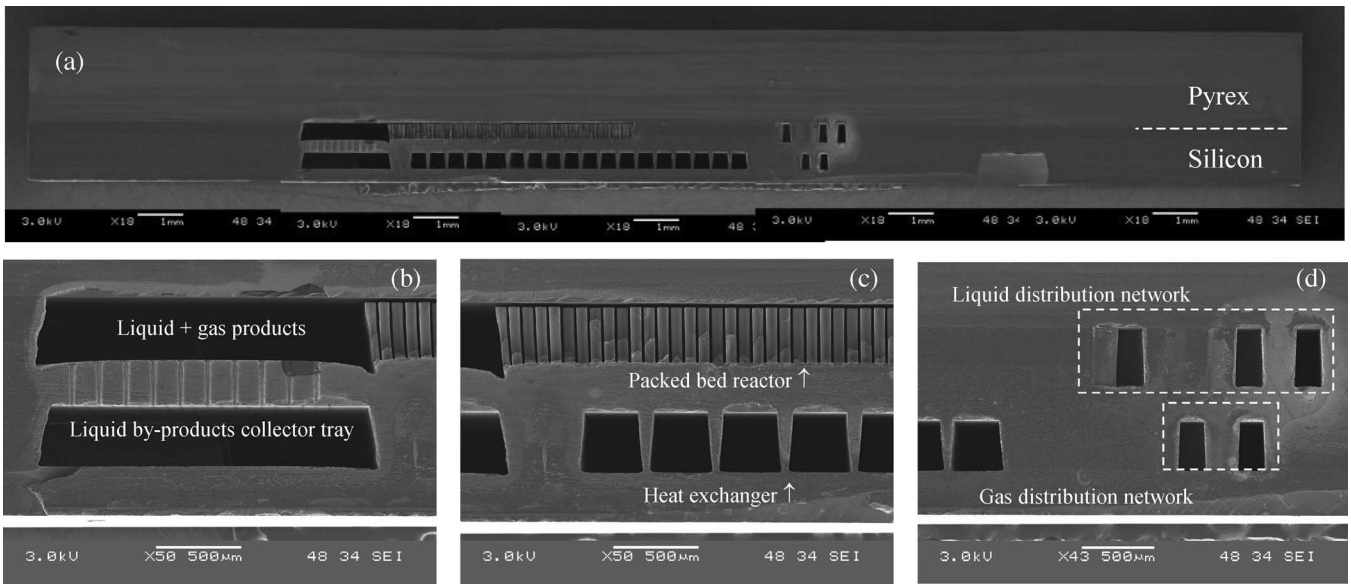

Fig. 8. (a) Set of SEM pictures that shows the cross section of a μSOG chip, with several key features highlighted: (b) separator; (c) packed-bed reactor and heat exchanger; and (d) reactant distribution network.

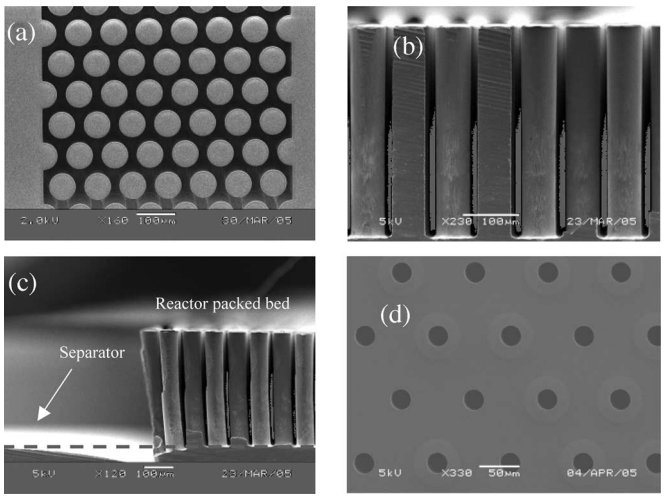

Fig. 9. (a) SEM of the top view of a reactor packed-bed channel. (b) Cross section of the reactor packed-bed channel. (c) Cross section of the separator near the end of the reactor array. (d) Top view of the capillary separator.

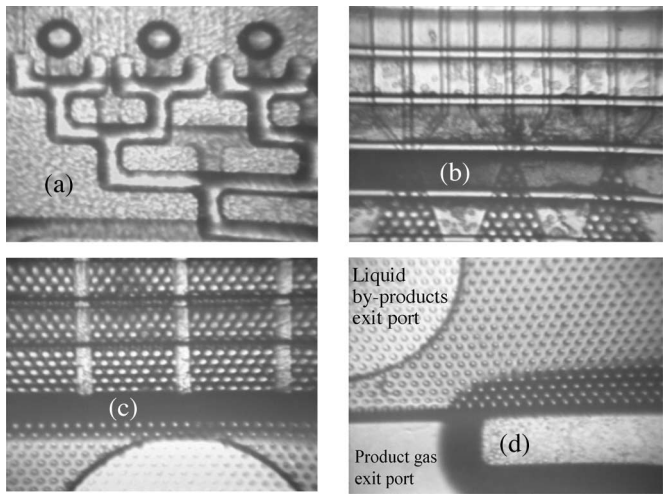

Fig. 10. Set of IR microscope images that show the structure of the μSOG chip. (a) Liquid and gas reactant manifolds. (b) Reactant injectors. (c) Reactor packed bed on top of the heat exchanger. (d) Capillary separator.

The DRIE recipe that patterned the packed bed is insensitive to microloading, i.e., the etch rate of the columns is the same as the etch rate of the open area where the separator is formed. Fig. 10 is a set of IR pictures that show the structure of the μSOG, including the reactant manifolds, the reactant injector structure (the gaseous reactant flow is surrounded by the liquid reactant flow at the entrance to the reaction channels), the reactor packed bed (the reactor is right on top of the cooling channels of the heat exchanger), the heat exchanger structure (there is a set of ribs to stiffen to the heat exchanger, as well as increase the surface area for better heat transfer), and the separator.

IV. Package

BHP and chlorine are very reactive, and the μSOG package materials must be selected for resistance to these chemicals (including resistance to chlorine in the presence of humidity). The μSOG package must also minimize the deactivation of $O_2(a)$ to maximize yield. To meet these requirements, connections to the μSOG chip were made with 1/8- and 1/16-in Teflon tubing, except for the gas outlet, which was directly connected to a quartz optical cell for $O_2(a)$ detection. Glass is ideal for the gas outlet because it permits optical access and has a $O_2(a)$ wall deactivation coefficient that is half that of the best metals and an order of magnitude lower than that of Teflon and, therefore, minimizes surface deactivation of $O_2(a)$ [9]. Minimizing $O_2(a)$ deactivation also requires that the gas outlet path have low-enough surface-to-volume ratio to ensure that wall deactivation is not a dominant $O_2(a)$ loss mechanism, while still having a short-enough residence time to ensure that homogeneous deactivation of $O_2(a)$ is as low as possible; the 2-mm-diameter entrance to the quartz optical cell is a good compromise between these two competing requirements. The package must also seal to the chip's ports, and the seal must

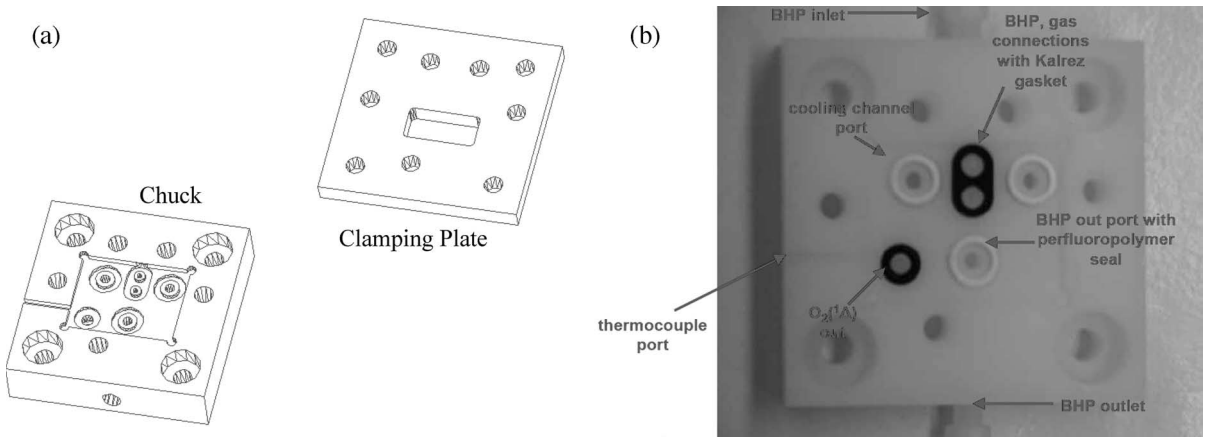

Fig. 11. (a) Three-dimensional drawing of the improved μSOG package. (b) Photograph of the package chuck with the o-ring and gaskets installed.

be leak-free over a wide range of internal chip pressures (from vacuum to several atmospheres). For the proof of concept demonstration shown in this paper, the connections were simply epoxied to the chip. For the systematic exploration of the performance space shown in Part II of this paper [10], the connections were made by means of a chemically-resistant, readily-machinable, stiff Tefzel package that seals to the chip with chemically resistant Simriz and Kalrez o-rings and gaskets. The package comprises a chuck (with o-ring ports to interface to the chip) that is clamped with Tefzel screws to a plate that includes an opening to permit optical access to the chip (Fig. 11). Finger-tight Tefzel fittings (Bio-Chem Valve Inc., Boonton, NJ) connect to the tubing to allow easy package reassembly.

V. Experimental Results

Prior to operation with Cl_2 and BHP, the μSOG's flow functionality was investigated using He and distilled (DI) water. The most important functionalities are the following: 1) the gas–liquid hydrodynamics in the packed-bed reaction channels and 2) the extent of liquid removal by the capillary separator. Both are critical to device performance, as effective mixing directly affects the rate of $O_2(a)$ generation and complete removal of the liquid by-products is necessary for the μSOG's use in a complete COIL system. In addition, although microscale packed-bed reaction channels and capillary separation have been demonstrated before (see, e.g., [6]–[8]), differences in the design and functionality of this system necessitate the flow characterizations that are described here. One key difference lies in the operating point of the capillary separator, which must operate with low pressures of 50–250 torr on the inlet side of the capillary separator instead of with the atmospheric pressure at the inlet as in [8]. Another key difference is the integration of the elements that are described here into a complete system.

Two unique modes of gas–liquid flow were observed in the present device. At low gas flow rates (below about 50 sccm), a steady flow pattern is observed in which the liquid continuously flows as a wetted film along the channel walls and partially wets the posts, while the gas flows through the remaining voids. Once developed, gas–liquid interfaces in this regime remain stationary with the majority of the reactor volume being occupied by the gas, resulting in a limited interaction between the two phases. At higher gas flow rates, the gas–liquid interface was observed to rapidly fluctuate, resulting in an unsteady liquid flow, which may enhance gas–liquid mixing. A steady flow was observed under all reacting conditions that were investigated.

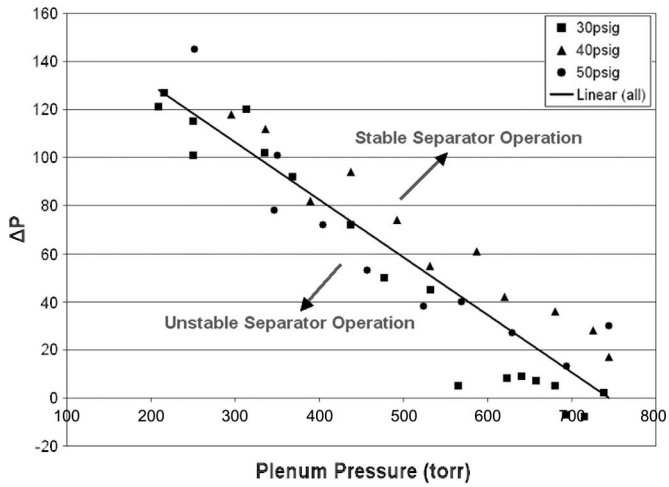

Fig. 12. Minimum applied pressure drop across the capillary pores that is necessary to ensure proper separator functionality, plotted versus plenum pressure for three liquid delivery pressures.

The capillary separator's performance was also investigated using He and DI water. As far as the authors are aware, this is the first reported demonstration of separation of a liquid–gas mixture below atmospheric pressure using the capillary micropore concept [8]. The separator operates on the basis of liquid capillary pressure; during operation, the pores are filled with liquid, which is driven through the holes and out of the chip by an externally imposed pressure drop. The capillary pressure of the liquid film resists the flow of gas through these same holes, thus effectively separating the two phases. A linear relationship was observed between the plenum pressure (the pressure at the phase separation point) and the minimum applied pressure drop across the capillary pores necessary to ensure phase separation. Fig. 12 illustrates this relationship for three different liquid delivery pressures, corresponding to three different liquid flow rates. No relationship between the liquid flow rate and the

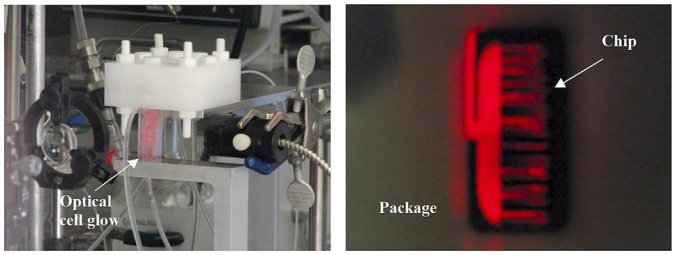

Fig. 13. Photographs of the dimol emission (red glow) from the μSOG in operation. (a) Dimol emission seen in the quartz optical cell. (b) Top view of the dimol emission from the chip while producing singlet delta oxygen.

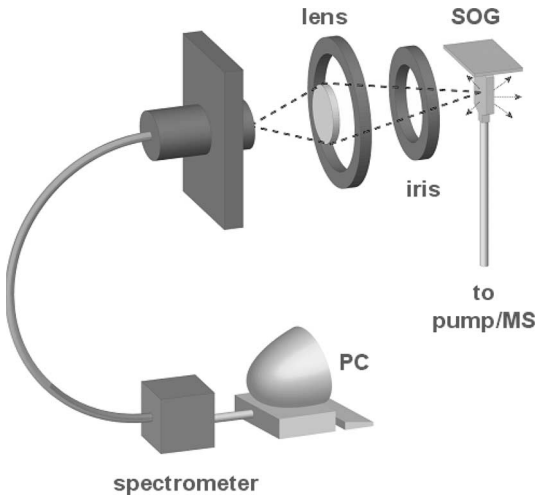

Fig. 14. Schematic of the system used to obtain IR spectra from the optical cell.

required pressure drop was observed, most likely because the liquid flow rates are significantly below the separator's designed capacity. Detailed models of the separator's performance are relevant for the quantitative analysis of the μSOG's performance across its operating space, and they are described in Part II of this paper [10].

Using the results of the water and He experiments, the chip was operated with BHP and chlorine flows to generate $O_2(a)$ using steady BHP flow and, typically, 1-min-long chlorine pulses. It is relatively straightforward to confirm $O_2(a)$ generation, but quantitatively measuring the yield is a significant challenge. A detailed account of the quantitative measurement of the $O_2(a)$ is presented in Part II of this paper [10]. Three measurement techniques were used to qualitatively verify the generation of $O_2(a)$. The first approach relies on the fact that two $O_2(a)$ molecules can collide to form a dimol. The subsequent dimol emission appears as a red glow (Fig. 13). In the second approach (Fig. 14), an optical system monitors the spontaneous decay of the $O_2(a)$ molecule to its ground state $O_2(X)$ and the resulting emission of a photon. The chip was operated under the experimental conditions that are described in Table I to demonstrate the proof of concept of the μSOG. Fig. 15 shows a typical spectral measurement. The spectrum is centered around the 1.268-μm wavelength of the $O_2(a)-O_2(X)$ emission. The IR spectral data in Fig. 15 have a signal-to-noise-ratio that is better than 12. Finally, the third approach consisted of analyzing the gas products by mass spectrometry.

TABLE I
EXPERIMENTAL CONDITIONS UNDER WHICH THE μSOG CHIP OPERATED FOR THE PROOF OF CONCEPT DEMONSTRATION. THESE PARTICULAR OPERATING CONDITIONS CORRESPOND TO THE SPECTRUM SHOWN IN FIG. 15

Parameter	Value
He Flowrate	37 sccm
Cl_2 Flowrate	13 sccm
BHP Flowrate	1 ml/min
BHP Delivery Pressure	40 psig
Plenum Pressure	100 torr
Separator Pressure	20 torr
Chip Temperature	3 C
BHP Supply Temperature	-10 C

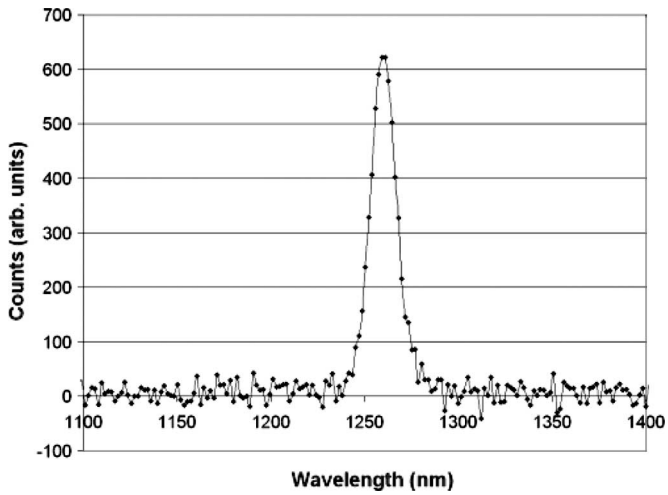

Fig. 15. Typical IR spectra of the emission coming out of the μSOG chip's quartz optical cell. The spectrum is mainly composed of photons from the $O_2(a)$ to O_2X transition.

A commercial mass spectrometer was used to measure the total molar fraction of oxygen (in all states of excitation combined) and, in particular, to capture the rise in the oxygen molar fraction above the background signal when chlorine is flowing. Fig. 16 shows the time variation of the oxygen molar fraction during two successive chlorine pulses. The rise in O_2 mole fraction correlates with the chlorine pulses and is clear evidence of oxygen production from the chip.

VI. CONCLUSION

The microfabrication and proof of concept demonstration of a MEMS-based SOG have been shown. The fabrication process for the μSOG is driven by the need to meet the device's stringent specifications in geometry, device uniformity, and chemical compatibility. This process has been shown to be robust, with typical yields of about 100%; the high repeatability offers the potential for future integration of arrays of μSOG chips to form singlet-oxygen-generating hardware that combines the total capacity of a macroscale SOG with the performance advantages of a MEMS-based system. The μSOG's generation of singlet delta oxygen has been qualitatively confirmed by the three complementary observations

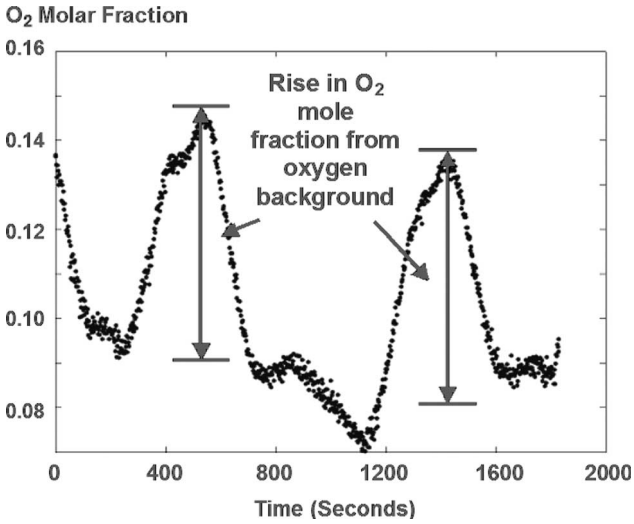

Fig. 16. Mass spectrometer signal indicating an increase in O_2, which coincides with the Cl_2 pulses.

of visible dimol emission, emission of 1268-nm photons as the singlet delta molecule spontaneously decays to the ground state, and increases in total oxygen in the output flow, as measured by mass spectrometry, which correlate with the chlorine feed.

ACKNOWLEDGMENT

The authors would like to thank J. Letendre for his expertise in building the experimental apparatus and D. Park for the help with images of the SOG and optics. Additionally, the microfabrication expertise of Dr. H. Li and the staff of the Microsystems Technology Laboratories at MIT was critical to the success of the project. All microfabrication was carried out in the Microsystems Technology Laboratories at MIT. The views and conclusions that are contained in this document are those of the authors and should not be interpreted as representing the official policies, either expressed or implied, of the DARPA or the U.S. Government.

REFERENCES

[1] H. H. Wasserman and R. W. Murray, *Singlet Oxygen*. New York: Academic, 1979, p. 25.
[2] W. E. McDermott *et al.*, "An electronic transition chemical laser," *Appl. Phys. Lett.*, vol. 32, no. 8, pp. 469–470, Apr. 1978.
[3] S. Yoshida, H. Saito, and T. Fujioka, "New singlet oxygen generator for chemical oxygen–iodine lasers," *Appl. Phys. Lett.*, vol. 49, no. 18, pp. 1143–1144, 1986.
[4] K. R. Kendrick *et al.*, "Determination of singlet-oxygen generator efficiency on a 10-kW class supersonic chemical oxygen–iodine laser (RADICL)," *IEEE J. Quantum Electron.*, vol. 35, no. 12, pp. 1759–1764, Dec. 1999.
[5] B. A. Wilhite *et al.*, "Design of a MEMS-based microchemical oxygen–iodine laser (μCOIL) system," *IEEE J. Quantum Electron.*, vol. 40, no. 8, pp. 1041–1055, Aug. 2004.
[6] M. W. Losey *et al.*, "Microfabricated multiphase packed-bed reactors: Characterization of mass transfer and reactions," *Ind. Eng. Chem. Res.*, vol. 40, no. 12, pp. 2555–2562, 2001.
[7] Y. Wada, M. A. Schmidt, and K. Jensen, "Flow distribution and ozonolysis in gas–liquid multichannel microreactors," *Ind. Eng. Chem. Res.*, vol. 45, no. 24, pp. 8036–8042, 2006.
[8] A. Günther *et al.*, "Micromixing of miscible liquids in segmented gas–liquid flow," *Langmuir*, vol. 21, no. 4, pp. 1547–1555, 2005.
[9] K. A. Truesdell, S. E. Lamberson, and G. D. Hager, "Phillips laboratory COIL technology overview," presented at the 23rd Plasmadynamics and Lasers Conf., Nashville, TN, Jul. 6–8, 1992, Paper AIAA 92-3003.
[10] T. F. Hill, L. F. Velásquez-García, B. A. Wilhite, K. F. Jensen, A. H. Epstein, and C. Livermore, "MEMS singlet oxygen generator—Part II: Experimental exploration of the performance space," *J. Microelectromech. Syst*. to be published.

Luis Fernando Velásquez-García received the bachelor's degrees in mechanical engineering (valedictorian of the School of Engineering, *magna cum laude*) and civil engineering (valedictorian of the School of Engineering, *magna cum laude*) from the Universidad de los Andes, Bogotá, Colombia, in 1998 and 1999, respectively, and the M.Sc. degree in aeronautics and astronautics and the Ph.D. degree in space propulsion from Massachusetts Institute of Technology (MIT), Cambridge, in 2001 and 2004, respectively.

In 2004, he was a Postdoctoral Associate with the Microsystems Technology Laboratories and the Gas Turbine Laboratory, MIT, where he has been a Research Scientist since 2005. His research interests include microfabrication and nanofabrication technologies applied to propulsion, analytical, and power systems. He has conducted research in microtechnology and nanotechnology applied to electrospray (internally and externally fed dense emitter arrays), plasma-enhanced chemical vapor deposited carbon-nanotube-based devices, 3-D packaging, mass spectrometry (quadrupole mass filters, electron impact ionizers, and field ionizers), and chemical reactors (monopropellant rockets and lasers).

Tyrone F. Hill received the B.S. degree in electrical engineering from the University of Illinois, Urbana-Champaign, in 2001 and the M.S. degree in electrical engineering from the Massachusetts Institute of Technology (MIT), Cambridge, in June 2004. He is currently working toward the Ph.D. degree in the Department of Electrical Engineering and Computer Science, MIT.

His research interests include MEMS fabrication techniques and optical emission diagnostics.

Benjamin A. Wilhite received the bachelor's degree in chemical engineering from North Carolina State University, Raleigh, in 1997 and the Ph.D. degree in chemical engineering from the University of Notre Dame, Notre Dame, IN, in 2003.

From 2002 to 2005, he was a Postdoctoral Research Associate and Research Scientist with the Massachusetts Institute of Technology, Cambridge. He is currently an Assistant Professor of chemical engineering with the Department of Chemical Engineering, University of Connecticut, Storrs. His research interests include chemical reaction engineering, multiphase transport, and membrane reformers, particularly in the development of portable chemistry systems and alternative energy processes operable from biofuels.

Klavs F. Jensen received the M.Sc. degree in chemical engineering from the Technical University of Denmark, Lyngby, and the Ph.D. degree in chemical engineering from the University of Wisconsin, Madison.

He is the Warren K. Lewis Professor and Head of Chemical Engineering and a Professor of materials science and engineering with the Massachusetts Institute of Technology (MIT). His research interests include the microfabrication, testing, integration, and scale-up of microfluidic systems for chemical and biochemical discovery, synthesis, and processing, chemical kinetics and transport phenomena related to the processing of organic and inorganic materials for electronic and optical applications, and the development of simulation approaches for reactive systems.

Prof. Jensen is a member of the U.S. National Academy of Engineering and a Fellow of the Royal Society of Chemistry. He serves on the steering committee of the International Conference on Miniaturized Systems for Chemistry and Life Sciences (μTAS) and was the Chair of μTAS 2005. He is the recipient of a U.S. National Science Foundation Presidential Young Investigator Award, a Guggenheim Fellowship, and the Allan P. Colburn, Charles C. M. Stine, and R. H. Wilhelm Awards of the American Institute of Chemical Engineers.

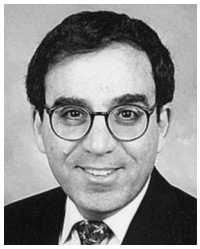

Alan H. Epstein received the S.B., S.M., and Ph.D. degrees in aeronautics and astronautics from the Massachusetts Institute of Technology (MIT), Cambridge.

He is currently the R. C. Maclaurin Professor of Aeronautics and Astronautics and Director of the Gas Turbine Laboratory at MIT. His research includes the fields of energy conversion, aero and rocket propulsion, and microsystems, specifically micropropulsion and energy conversion devices.

Dr. Epstein is a member of American Society of Mechanical Engineers (ASME), a Fellow of the American Institute of Aeronautics and Astronautics (AIAA), and a member of the National Academy of Engineering.

Carol Livermore (M'98) received the B.S. degree in physics from the University of Massachusetts, Amherst, in 1993 and the A.M. and Ph.D. degrees in physics from Harvard University, Cambridge, in 1995 and 1998, respectively.

From 1998 to 2002, she was first a Postdoctoral Associate and then a Research Scientist with the Massachusetts Institute of Technology (MIT), Cambridge. She is currently a Singapore-MIT Alliance (SMA) Assistant Professor of manufacturing with the Department of Mechanical Engineering, MIT. Her current research interests include power MEMS and the development of techniques and applications for nanoscale and microscale self assembly.

Dr. Livermore is a member of the American Society of Mechanical Engineers.